




Cite this: *Chem. Commun.*, 2025, 61, 15830

Received 19th July 2025,  
Accepted 4th September 2025

DOI: 10.1039/d5cc04076k

rsc.li/chemcomm

# High-performance ceria *via* supramolecular metal–organic gel precursors for visible-light-driven hydrogen evolution from aqueous glucose

Andrea Muscatello,<sup>a</sup> Giuseppina Iervolino,<sup>\*b</sup> Vincenzo Vaiano<sup>b</sup> and Serena Esposito <sup>\*a</sup>

**A supramolecular cerium-based metal–organic gel (MOG) was used as a soft precursor to prepare a defect-rich CeO<sub>2</sub> photocatalyst. The resulting material exhibited enhanced visible-light-driven hydrogen evolution from glucose, outperforming conventionally synthesized ceria. Spectroscopic analysis revealed higher oxygen vacancy content and improved charge separation, highlighting the potential of MOG-derived photocatalysts.**

Hydrogen is a promising alternative to fossil fuels due to its high energy density and carbon-free combustion. Among various production methods, photocatalysis has attracted considerable attention for its ability to harness solar energy, an abundant and renewable resource. Certain food-processing wastewaters are particularly rich in glucose and other sugars, providing a biomass-derived feedstock for sustainable hydrogen generation. In this context, photocatalytic hydrogen production *via* glucose decomposition in aqueous solution has emerged as a low-cost and practical strategy to support the transition to hydrogen-based energy systems.<sup>1–4</sup> The development of efficient photocatalytic systems for this purpose relies heavily on the design of advanced functional materials. In this scenario, metal–organic gels (MOGs) have recently gained interest as versatile precursors for oxide-based photocatalysts, owing to their tuneable structural and textural properties. Indeed, MOGs represent an intriguing class of soft materials, structurally related to metal–organic frameworks (MOFs) but generally less ordered. MOGs form *via* rapid aggregation of metal–ligand clusters under supramolecular interactions, though some degree of coordinative cross-linking may occur.<sup>5–9</sup> The synthesis of MOGs is characterized by mild reaction conditions, simplicity of equipment, and low production costs. This ease of fabrication, combined with the

flexibility in self-assembly of the diverse building blocks, provides significant versatility in achieving targeted structural control and functional diversification. These attributes position MOGs as highly attractive materials for advanced applications.<sup>10,11</sup> In this scenario, careful tuning of the synthesis parameters becomes crucial, as it enables precise control over supramolecular self-assembly across multiple length scales, leading directly to the preparation of targeted gel architectures. Key parameters include the choice of metal source, water content, and reactant concentrations.<sup>12,13</sup>

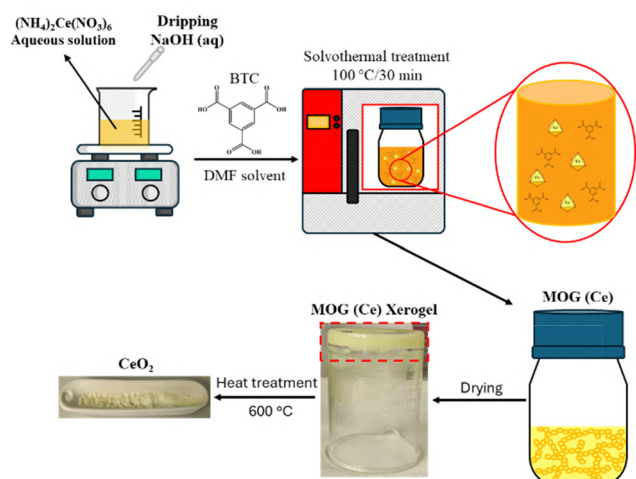
One of the most compelling aspects of MOGs lies in their potential as sacrificial templates for the synthesis of advanced functional materials, particularly metal oxides.<sup>14</sup> Through controlled thermal treatments, such as combustion or pyrolysis, the organic components of the MOG can be removed, leaving behind the metal oxide while largely preserving the nanoscale architecture and homogeneity inherited from the parent gel.<sup>15</sup> The “gel-to-oxide” transformation offers significant advantages over traditional synthesis methods, allowing for precise control over structural, surface and textural properties, which are critical parameters for optimizing material performance.<sup>10,16–18</sup> Specifically, we aim to exploit the intrinsic properties of MOGs to prepare highly efficient CeO<sub>2</sub> photocatalysts for hydrogen evolution from aqueous solutions containing organic sacrificial agents (*e.g.*, glucose), as CeO<sub>2</sub> is known to promote photocatalytic hydrogen production from a variety of organic compounds in aqueous media.<sup>19,20</sup>

Herein, we propose the synthesis of cerium dioxide nanoparticles *via* the controlled combustion of a cerium-based metal–organic gel. The MOG precursor was prepared using a one-pot solvothermal approach where (NH<sub>4</sub>)<sub>2</sub>Ce(NO<sub>3</sub>)<sub>6</sub> and benzene-1,3,5-tricarboxylic acid (BTC) were selected as building blocks. A systematic variation of the synthesis parameters, such as cerium precursor concentration, the Ce:BTC molar ratio, the molar amount of NaOH, and the quantity of DMF solvent, was adopted to control gel formation, specifically distinguishing between flowing and non-flowing gel states. This

<sup>a</sup> Department of Applied Science and Technology, Politecnico di Torino, Corso Duca degli Abruzzi 24, 10129 Torino, Italy. E-mail: serena\_esposito@polito.it

<sup>b</sup> Department of Industrial Engineering, University of Salerno, Via Giovanni Paolo II 132, 84084 Fisciano, SA, Italy. E-mail: giervolino@unisa.it





**Scheme 1** Scheme of the preparation route of MOG (Ce) and derived CeO<sub>2</sub>-MOG by heat treatment in air.

meticulous investigation allowed us to precisely understand the impact of each variable on the gelation process, enabling the optimization of the synthesis procedure (see SI “Summary of the systematic variation of synthesis parameters”). The MOG gel precursor was characterized by thermogravimetric analysis (TGA) and X-ray diffraction (XRD) to confirm its thermal and structural properties (Fig. S1 and S2, SI). This optimized approach directly led to the successful formation of the Ce-MOG xerogel after solvent removal, as depicted in Scheme 1. Subsequently, the Ce-MOG xerogel was calcined in air at temperatures up to 600 °C to yield cerium oxide. This temperature was selected based on TGA analysis of the gel (Fig. S1, SI). To highlight the advantages of our approach, the resulting CeO<sub>2</sub>-MOG was directly compared with CeO<sub>2</sub>-P, a reference ceria sample prepared *via* the conventional precipitation method.

Highly crystalline cerium oxide with its characteristic fluorite structure was successfully obtained by combustion of Ce-MOG, as confirmed by comparison with CeO<sub>2</sub>-P (Fig. S3, SI).

Crucially, this synthesis pathway *via* the MOG precursor resulted in a material with markedly different textural properties compared to the conventionally prepared CeO<sub>2</sub>-P, highlighting the profound influence of the synthesis route on the final catalyst characteristics.

While both catalysts exhibit type II N<sub>2</sub> adsorption-desorption isotherms at 77 K (Fig. S4, SI), their contrasting hysteresis loops reveal distinct porous textures. The MOG-derived ceria displays an H3-type hysteresis, consistent with a more open mesoporous network, while the precipitated sample shows an H4-type loop, typically associated with narrow slit-like pores and the presence of microporosity. Textural data are summarized in Table 1. The CeO<sub>2</sub>-P showed a relatively high specific surface area (SSA) of 81 m<sup>2</sup> g<sup>-1</sup> but a low total pore volume of 0.05 cm<sup>3</sup> g<sup>-1</sup>, suggesting the predominance of small pores likely in the microporous to narrow mesoporous range. In contrast, the CeO<sub>2</sub>-MOG exhibited a significantly lower SSA of 22 m<sup>2</sup> g<sup>-1</sup> but a higher total pore volume of 0.1 cm<sup>3</sup> g<sup>-1</sup>,

**Table 1** Summary of the textural data of catalysts prepared by MOG combustion and conventional precipitation

	SSA (m <sup>2</sup> g <sup>-1</sup> )	Micropore volume (cm <sup>3</sup> g <sup>-1</sup> )	External surface area (m <sup>2</sup> g <sup>-1</sup> )	Total pore volume (cm <sup>3</sup> g <sup>-1</sup> )
CeO <sub>2</sub> -MOG	22	0.0008	19.8	0.10
CeO <sub>2</sub> -P	81	0.0033	73.3	0.05

indicative of a mesoporous or even partially macroporous structure.

Fig. 1a shows the Raman spectra of the CeO<sub>2</sub>-MOG and CeO<sub>2</sub>-P samples. Both spectra exhibit a prominent peak at ~465 cm<sup>-1</sup>, which corresponds to the F<sub>2g</sub> symmetric stretching mode of the fluorite cubic phase of CeO<sub>2</sub>,<sup>21,22</sup> confirming the formation of crystalline ceria in both materials. Notably, CeO<sub>2</sub>-MOG displays a broader signal, indicating a greater degree of structural disorder. In addition, the CeO<sub>2</sub>-MOG spectrum reveals distinct defect-related D-modes in the 550–650 cm<sup>-1</sup> region, which are significantly less pronounced in the CeO<sub>2</sub>-P sample. These features are typically associated with oxygen vacancies and lattice defects,<sup>23</sup> suggesting that the MOG-derived synthesis route promotes the formation of a more defective ceria network. The defect content was qualitatively assessed by the intensity ratio between the D-mode (~600 cm<sup>-1</sup>) and the F<sub>2g</sub> mode (~465 cm<sup>-1</sup>). The I<sub>D</sub>/I<sub>F2g</sub> ratio

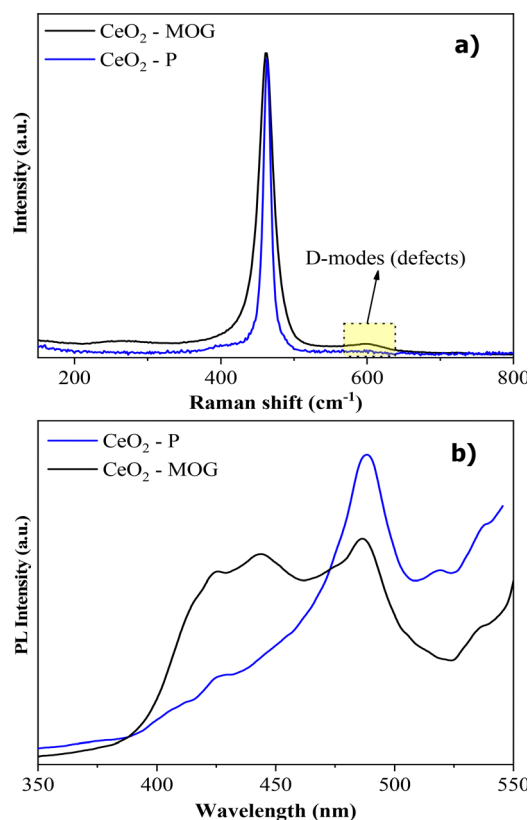


**Fig. 1** (a) Raman spectra of CeO<sub>2</sub>-P and CeO<sub>2</sub>-MOG photocatalysts. (b) Photoluminescence spectra of CeO<sub>2</sub>-P and CeO<sub>2</sub>-MOG samples.



increases from  $\sim 0.002$  for  $\text{CeO}_2\text{-P}$  to  $\sim 0.004$  for  $\text{CeO}_2\text{-MOG}$ , indicating a higher density of structural defects in the latter; this ratio is routinely used to assess the oxygen vacancy level in ceria-based materials.<sup>24</sup> Critical insights into the defect and electronic structure were provided by photoluminescence spectroscopy (PL) (Fig. 1b). This technique, which reveals information on electron-hole pair dynamics, confirms the existence of defect energy levels within the band gap, attributed to both  $\text{Ce}^{3+}$  sub-bands and oxygen vacancies. Nevertheless, the emission spectra of  $\text{CeO}_2\text{-P}$  and  $\text{CeO}_2\text{-MOG}$  revealed distinct peak profiles. The most intense peak at 488 nm (green-blue region), attributable to  $\text{F}^{+*} \rightarrow \text{F}^+$  emission, where  $\text{F}^+$  is defect state related to oxygen vacancies containing 1 electron and  $\text{F}^{+*}$  is an excited state close to the conduction band, is notably less intense for  $\text{CeO}_2\text{-MOG}$ .<sup>25</sup> This reduced intensity indicates an increased carrier lifetime in  $\text{CeO}_2\text{-MOG}$ , suggesting different recombination dynamics and, potentially, a greater availability of electrons for surface redox processes.

Another noteworthy feature of the  $\text{CeO}_2\text{-MOG}$  sample is the richer presence of bands in the 380–460 nm range, which are hardly visible in  $\text{CeO}_2\text{-P}$ . Specifically, the bands at 425 nm and 443 nm are associated with the  $\text{Ce}^{3+} 4\text{f}^1$  state located 1.3–1.5 eV above the valence band.<sup>26</sup> This suggests that  $\text{CeO}_2\text{-MOG}$  possesses a more defective nature compared to the  $\text{CeO}_2\text{-P}$  sample. The time-resolved  $\text{H}_2$  production profiles for  $\text{CeO}_2\text{-P}$  and  $\text{CeO}_2\text{-MOG}$  are reported in Fig. 2; for direct comparison, the values at 240 minutes of visible-light irradiation were considered.  $\text{CeO}_2\text{-MOG}$  exhibits a significantly higher  $\text{H}_2$  evolution rate than the reference  $\text{CeO}_2\text{-P}$ , reaching over  $11\,000\ \mu\text{mol L}^{-1}$  after 240 minutes.

This clearly highlights the superior photocatalytic performance of  $\text{CeO}_2\text{-MOG}$ , underscoring how synthesis conditions are paramount in tailoring the functional features of  $\text{CeO}_2$ -based catalysts. Given their nearly identical band gap energies ( $\sim 2.96$  eV as shown by Tauc plot (Fig. S5, SI)), differences in visible-light absorption cannot account for the improved

photocatalytic activity of  $\text{CeO}_2\text{-MOG}$ . Instead, the improved performance is closely related to the structural and electronic properties of the material. Raman spectroscopy (Fig. 1a) reveals a more intense signal in the  $550\text{--}650\ \text{cm}^{-1}$  region for  $\text{CeO}_2\text{-MOG}$ , indicative of a higher concentration of oxygen vacancies.

This is corroborated by PL measurements (Fig. 1b), where  $\text{CeO}_2\text{-MOG}$  shows markedly lower emission intensity compared to  $\text{CeO}_2\text{-P}$ , suggesting reduced radiative recombination of photogenerated carriers. Moreover, the broader and slightly red-shifted PL band observed for  $\text{CeO}_2\text{-MOG}$  implies the presence of defect-related sub-bandgap states, such as  $\text{Ce}^{3+}$  sites and oxygen vacancy levels, which can trap charge carriers and prolong their lifetime, thereby enhancing the probability of interfacial redox reactions. These observations are in line with previous findings on oxygen vacancy-rich  $\text{CeO}_2$ -based photocatalysts, which demonstrated enhanced  $\text{H}_2$  evolution efficiency due to defect-mediated charge transport pathways.<sup>27</sup> In addition to its superior  $\text{H}_2$  evolution,  $\text{CeO}_2\text{-MOG}$  also exhibited a higher  $\text{CO}_2$  production compared to  $\text{CeO}_2\text{-P}$  under the same reaction conditions. The time-resolved  $\text{CO}_2$  production profiles are reported in Fig. S6 (SI). This observation suggests a more efficient and complete oxidative decomposition of the organic sacrificial agent (*e.g.*, glucose), which is consistent with the enhanced photocatalytic activity of the MOG-derived material. The increased  $\text{CO}_2$  yield supports the hypothesis that  $\text{CeO}_2\text{-MOG}$  promotes more effective charge carrier separation and utilization, facilitating both reduction ( $\text{H}_2$  evolution) and oxidation (organic degradation) half-reactions.

The reusability of the  $\text{CeO}_2\text{-MOG}$  photocatalyst was assessed over six consecutive photocatalytic cycles under visible-light irradiation (Fig. 3). After each 4-hour cycle, the catalyst was recovered by centrifugation, thoroughly washed with deionized water, and dried before reuse. As shown in Fig. 3,  $\text{CeO}_2\text{-MOG}$  retained nearly constant hydrogen production throughout all six cycles, with a negligible decrease in activity ( $< 2\%$ ), well

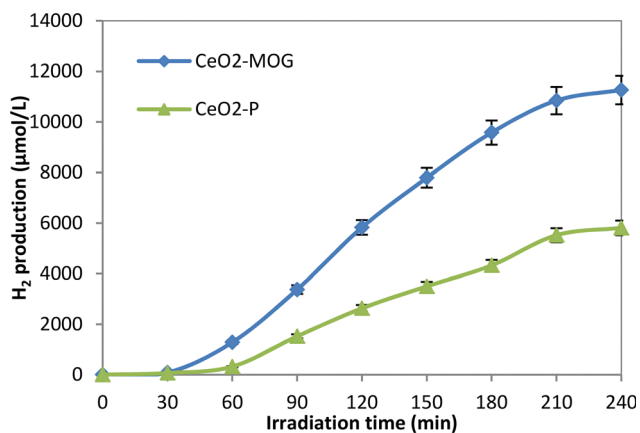


Fig. 2 Hydrogen production over  $\text{CeO}_2\text{-P}$  (prepared with conventional precipitation synthesis), and  $\text{CeO}_2\text{-MOG}$  photocatalysts during 4 hours of visible light irradiation. Reaction conditions: catalyst dosage =  $2\ \text{g L}^{-1}$ ; initial glucose concentration =  $250\ \text{mg L}^{-1}$ ; solution volume =  $80\ \text{mL}$ ; light source = four visible light lamps (8 W each, 400–700 nm).

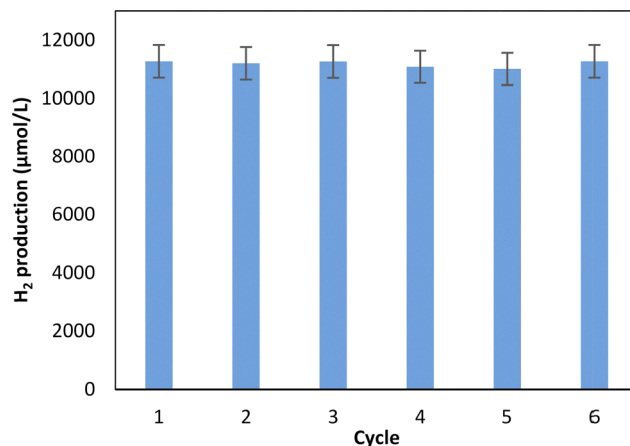


Fig. 3 Reusability test of  $\text{CeO}_2\text{-MOG}$  for photocatalytic hydrogen production under visible-light irradiation over six consecutive cycles. Reaction conditions: glucose concentration =  $250\ \text{mg L}^{-1}$ ; catalyst dosage =  $2\ \text{g L}^{-1}$ ; solution volume =  $80\ \text{mL}$ ; irradiation time = 4 hours per cycle; light source = four visible-light lamps (8 W each, 400–700 nm).



within the experimental margin of error. This excellent cycling stability underscores the structural and chemical robustness of the CeO<sub>2</sub>-MOG material under the adopted operational conditions.

In summary, a supramolecular metal–organic gel was successfully employed as a soft template for the synthesis of defect-rich CeO<sub>2</sub> nanoparticles, enabling enhanced photocatalytic hydrogen production from glucose under visible-light irradiation. Compared to conventionally prepared ceria, the MOG-derived catalyst exhibited a higher concentration of oxygen vacancies, improved charge carrier separation, and superior overall activity. The excellent recyclability over multiple cycles further highlights the robustness of the material under operating conditions. These findings demonstrate the potential of MOG-based routes for the rational design of advanced metal oxide photocatalysts for sustainable hydrogen generation from biomass-derived organics.

## Conflicts of interest

There are no conflicts to declare.

## Data availability

The data supporting this article have been included as part of the SI. Supplementary information: Experimental, and details of the results. See DOI: [10.1039/d5cc04076k](https://doi.org/10.1039/d5cc04076k).

## Notes and references

- 1 A. Mancuso and G. Iervolino, *Catalysts*, 2022, **12**, 1074.
- 2 Y. Li, J. Wang, S. Peng, G. Lu and S. Li, *Int. J. Hydrogen Energy*, 2010, **35**, 7116–7126.
- 3 X. Fu, J. Long, X. Wang, D. Y. Leung, Z. Ding, L. Wu, Z. Zhang, Z. Li and X. Fu, *Int. J. Hydrogen Energy*, 2008, **33**, 6484–6491.
- 4 K. A. Davis, S. Yoo, E. W. Shuler, B. D. Sherman, S. Lee and G. Leem, *Nano convergence*, 2021, **8**, 6.
- 5 J. Zhang and C.-Y. Su, *Coord. Chem. Rev.*, 2013, **257**, 1373–1408.
- 6 B. Zhang, J. Zhang, Y. Zhang, Q. Zuo and H. Zheng, *Langmuir*, 2023, **39**, 10892–10903.
- 7 L. Casimiro, F. Volatron, G. Boivin, B. Abécassis, S. Alves, D. Brouiri, D. Montero, J.-M. Guigner, L.-M. Chamoreau and G. Gontard, *JACS Au*, 2024, **4**, 4948–4956.
- 8 B. Bueken, N. Van Velthoven, T. Willhammar, T. Stassin, I. Stassen, D. A. Keen, G. V. Baron, J. F. Denayer, R. Ameloot and S. Bals, *Chem. Sci.*, 2017, **8**, 3939–3948.
- 9 J. Hou, A. F. Sapnik and T. D. Bennett, *Chem. Sci.*, 2020, **11**, 310–323.
- 10 S. Ma, J. Xu, S. Sohrabi and J. Zhang, *J. Mater. Chem. A*, 2023, **11**, 11572–11606.
- 11 Z. Zhuang, Z. Mai, T. Wang and D. Liu, *Coord. Chem. Rev.*, 2020, **421**, 213461.
- 12 F. Zhao, W. Yang, Y. Han, X. Luo, W. Tang, T. Yue and Z. Li, *Chem. Eng. J.*, 2021, **407**, 126744.
- 13 Z. Lin, J. J. Richardson, J. Zhou and F. Caruso, *Nat. Rev. Chem.*, 2023, **7**, 273–286.
- 14 J.-C. Huang, Y.-H. Shih, S. Lirio, S.-Y. Wu, H.-T. Chen, W.-L. Liu, C.-H. Lin and H.-Y. Huang, *Chem. Commun.*, 2019, **55**, 4475–4478.
- 15 Z. Cao, Z. Jiang, Y. Li, C. Huang and Y. Li, *ChemSusChem*, 2019, **12**, 2480–2486.
- 16 H. Wang, B. H. Chen and D. J. Liu, *Adv. Mater.*, 2021, **33**, 2008023.
- 17 N. Clayden, A. Aronne, S. Esposito and P. Pernice, *J. Non-Cryst. Solids*, 2004, **345**, 601–604.
- 18 S. Esposito, *Sol-Gel Synthesis Strategies for Tailored Catalytic Materials*, Springer, 2023, pp. 33–41.
- 19 G. Iervolino, V. Vaiano, D. Sannino, F. Puga, J. A. Navío and M. C. Hidalgo, *Catalysts*, 2021, **11**, 1558.
- 20 A. A. Yadav, Y. M. Hunge and S.-W. Kang, *Catalysts*, 2022, **12**, 1185.
- 21 W. Weber, K. Hass and J. McBride, *Phys. Rev. B: Condens Matter Mater. Phys.*, 1993, **48**, 178.
- 22 E. Sediva, A. J. Carrillo, C. Halloran and J. L. Rupp, *ACS Appl. Energy Mater.*, 2021, **4**, 1474–1483.
- 23 V. Araújo, W. Avansi, A. H. de Carvalho, M. Moreira, E. Longo, C. Ribeiro and M. I. B. Bernardi, *CrystEngComm*, 2012, **14**, 1150–1154.
- 24 F. Liu, Z. Wang, D. Wang, D. Chen, F. Chen and X. Li, *Catalysts*, 2019, **9**, 288.
- 25 G. Iervolino, O. Tammaro, M. Fontana, B. Masenelli, A. D. Lamirand, V. Vaiano and S. Esposito, *J. Energy Chem.*, 2025, **101**, 263–277.
- 26 K. Sudarshan, V. Tiwari, P. Utpalla and S. Gupta, *Inorg. Chem. Front.*, 2019, **6**, 2167–2177.
- 27 Y.-P. Qiu, W.-Z. Wang, M.-H. Chen, Q. Shi, Z.-Q. Yang and P. Wang, *J. Mater. Chem. A*, 2021, **9**, 18385–18392.

